Dynamic observations of deformation in an ultrafine-grained Al–Mg alloy with bimodal grain structure

Byungmin Ahn[1*], Enrique J. Lavernia[2] and Steven R. Nutt[1]

1. Department of Chemical Engineering and Materials Science, University of Southern California, Los Angeles, CA, 90089-0241, United States
2. Department of Chemical Engineering and Materials Science, University of California, Davis, CA, 95616-5294, United

[*]Email: byungahn@usc.edu

Abstract: The tensile properties and deformation response of an ultrafine-grained (UFG) Al–Mg alloy with bimodal grain structure were investigated using a micro-straining unit and a strain mapping technique. Atomized Al 5083 powder was ball-milled in liquid N2 to obtain a nanocrystalline (NC) structure, then blended with 50 wt.% unmilled coarse-grained (CG) powder, and consolidated to produce a bimodal grain structure. The blended powder was hot vacuum degassed to remove residual contaminants, consolidated by cold isostatic pressing (CIP), and then quasi-isostatic (QI) forged twice. The resultant material consisted of a UFG matrix and CG regions. The dynamic response during tensile deformation was observed using a light microscope, and the surface displacements were mapped and visualized using a digital image correlation (DIC) technique. The DIC results showed inhomogeneous strain between the UFG and CG regions after yielding, and the strain was localized primarily in the CG regions. Strain hardening in the CG regions accompanied the localization and was confirmed by variations in Vickers hardness.

1. Introduction

Bulk nanocrystalline materials (BNMs) have received increasing attention because of the enhancement of mechanical properties and the potential for structural applications. For example, BNMs exhibit enhanced strength compared with conventional materials [1–3], and the phenomenon is attributed to the fine grain size on the basis of the Hall-Petch mechanism [4, 5]. Different techniques have been developed to produce NC or UFG structures, including mechanical alloying [6, 7], severe plastic deformation [8], gas-phase condensation [9], and electrodeposition [10]. However, BNMs generally exhibit unacceptably low ductility and toughness, greatly limiting their widespread practical utility. Different processing approaches have been proposed to improve these properties [11–14]. In one such approach, the microstructural modification led to a multi-scale microstructure characterized by a bimodal grain structure [15, 16]. The microstructure contained micron-sized CG regions embedded in an NC matrix. The bimodal alloys reportedly showed improved ductility and toughness with only a modest decrease in strength when compared to the purely NC control alloy [15, 16]. The resulting properties have generated strong interest, although the fundamental mechanisms of plastic deformation of the bimodal alloys are not well understood.

Cryomilling, which refers to ball milling in a cryogenic fluid (typically liquid nitrogen), is a particularly effective process for producing NC powders, both in small batches (100's of grams) and commercial quantities (30–40 kg), while minimizing heat generation and oxygen contamination [7]. In this process, the powder particles are repeatedly sheared, fractured, and cold-welded over a period of several hours. The cryomilled powder is subsequently hot-vacuum degassed to remove process control agents and other contaminants. For primary consolidation, hot isostatic pressing (HIP), is often employed to achieve high compaction density. However, the HIP process often causes undesired grain growth, and CIP is sometimes employed to avoid this. Although CIPped materials

exhibit lower green-body density (~80%), the CIP process effectively prevents grain growth, and greatly reduces the cost and time of processing. In this study, CIP consolidation was followed by quasi-isostatic (QI) forging [17, 18] to break up prior particle boundaries (PPBs) remaining after CIP. During QI forging, the uniaxial pressure was transformed into a QI pressure field by the application of a granular pressure transmitting medium, and this introduced an additional shear stress which helped to break up PPBs in the bimodal alloys.

The unusual bimodal grain structure of the resulting alloys raises some interesting questions concerning the distribution of strain during deformation. DIC is a non-contacting strain field measuring technique that relies on mathematical correlation of digital images recorded during deformation under an applied load. For the last few decades, DIC has been developed to analyze and to visualize the actual strain and deformation of materials [19]. In the present case, two-dimensional (2D) DIC was performed using a high resolution digital camera coupled with a light microscope, and it was used to measure surface displacements of planar specimens. In the 2D DIC process, a computer-aided correlation is carried out using a pair of sequential images to determine surface displacements, which are recognized by movement of speckle patterns in digital images.

2. Experimental procedures

2.1. Material

Gas-atomized 325 mesh (<44 μm) Al 5083 (Al–4.4Mg–0.7Mn–0.15Cr wt.%) powder (produced by Valimet, Inc.) was cryomilled in a 20 kg batch by DWA Aluminum Composites for 8 h in a modified Szegvari attritor. Stainless steel balls with a diameter of 6.4 mm were used with a ball-to-powder weight ratio of 32:1. To improve milled powder yield, 0.2 wt.% of stearic acid was added. The cryomilled powders were combined and mechanically blended with 50 wt.% non-cryomilled

gas-atomized Al 5083 powder in an inert atmosphere to achieve a uniform distribution of bimodal microstructure. The blended powder was degassed at 450 °C under a vacuum of 10−6 Torr, and the degassed powder was transferred to a rubber CIP bag inside a glove box filled with dry nitrogen, then consolidated by CIP at 310 MPa pressure by Pittsburgh Materials Technology, Inc. The resulting CIPped billet was dry-machined to a cylindrical shape, 5 cm (D) × 12.7 cm (L). The CIPped billet was sealed in an Al 6061 can, pre-heated for 2 h at 454 °C, and then quasi-isostatically forged (Advance Materials & Manufacturing Technologies, LLC). After the first forging, the billet was re-heated to 454 °C for half an hour, then secondarily forged at 180° to the original direction. Final dimensions of the material were 6 cm (D) × 5 cm (L).

2.2. Tensile tests and hardness measurements

Two tensile specimens were prepared from the as-forged material to achieve a flat "dog-bone" shape. The gauge section was perpendicular to the forging direction with the dimensions of 4 mm (L) × 2.5 mm (W) × 1.5 mm (H). To confine the area of stress concentration for dynamic observation, two notches were introduced in the middle of the gauge section on opposite sides, as shown in Fig. 1a. The first specimen was used to acquire the nominal stress–strain curve, and the second one was used for hardness measurements during multiple intermissions during a tensile test. The specimens were mechanically polished to obtain mirror-like surfaces and then lightly etched for subsequent observation of the bimodal grain structure.

A micro-tensile stage module (Deben, UK) was utilized for the tests. The module was specifically designed to facilitate observation of micro-strain in microscopes. All tensile tests were performed at room temperature with a displacement rate of 1.67 μm/s, which, for the custom designed specimens in this study, was approximately equivalent to a strain rate of 4.18×10^{-4} s−1. The stage module was attached to a light microscope (Olympus Vanox AHMT3) as shown in Fig.

1b, and the dynamic deformation during the tensile test was sequentially recorded at time intervals of half a second using a digital camera (QICam 12-bit, QImaging Corp.) installed with the light microscope.

For hardness measurements, a tensile test was interrupted before fracture at different tensile stresses (0, 182, 364, 455, and 515 MPa). The Vickers hardness of both UFG regions and CG regions was obtained at each intermission using a microhardness tester (Future-Tech Corp). The indentations were made on two different locations on the gauge section—adjacent to the notches and in the central part between the notches—using a 10 gf load and a dwell time of 15 s.
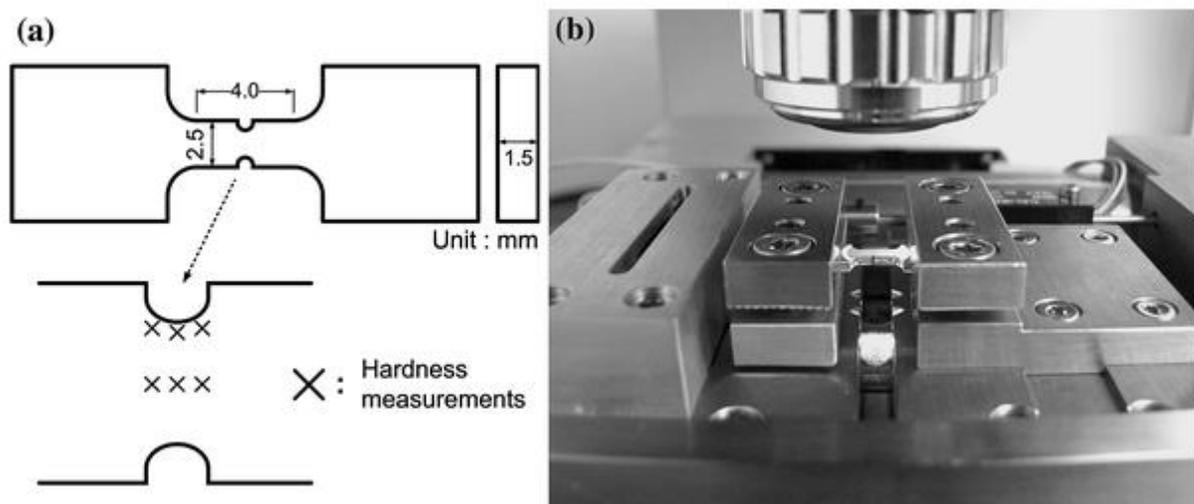

*Fig. 1 (**a**) Geometry of the specimen with notches; (**b**) Micro-tensile stage module attached to a light microscope*

2.3. Digital image correlation (DIC)

To measure the displacements that developed during tensile deformation, pairs of micrographs were recorded and selected. Each pair consisted of a reference and a deformed image within a range of both large strain and micro-strain, and the resolution of digital images was 1392×1040 pixels. Two-dimensional digital image correlation was performed using software (VIC-2D, Correlated

Solution, Inc.) with a subset size of 41 × 41 pixels, a step spacing of 5 pixels, and a linear subset shape function.

2.4. Electron microscopic investigation

Details of the microstructures were characterized by transmission electron microscopy (TEM) and scanning electron microscopy (SEM). The TEM was used to investigate the bimodal grain structure, and the specimens were prepared by electrolytic twin jet polishing in an ethanol solution containing 8% perchloric acid + 10% 2-butoxyethanol at a temperature of −40 °C. The number-based mean grain size was obtained directly from TEM images by measuring ~400 individual grains. The fracture surface of the tensile specimen was examined by SEM (Hitachi S-4800 FE-SEM).

3. Results and discussion

Figure 2 shows an optical micrograph and a TEM bright field image of as-forged material. The bimodal grain structure is apparent, and consists of a UFG matrix and CG regions (light contrast). In general, the CG areas were uniformly distributed in the UFG matrix, as shown in Fig. 2a. However, the PPBs of CG particles were not completely removed during the consolidation, as shown in Fig. 2a, which can adversely affect the ductility and toughness. The grains were elongated perpendicular to the forging direction, as shown in Fig. 2b. The mean grain size was 247 nm for UFG regions and ~4 μm for CG regions in the bimodal microstructure. As reported previously, the as-cryomilled powder exhibited a mean grain size of 50 nm with a narrow size distribution, although some grains were as large as 200 nm [20]. However, most of the nanosized grains produced by cryomilling underwent limited grain growth during consolidation. (Although CIP was employed for

primary consolidation in lieu of HIP, post-CIP processing included hot degassing and forging, which involved moderately high temperatures.)
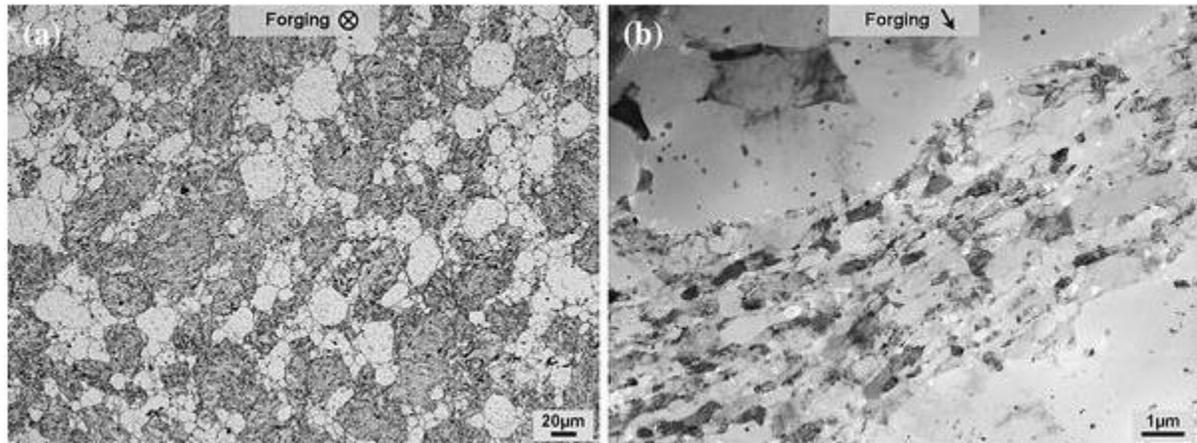

***Fig. 2** **(a)** Optical micrograph (etched) of the as-forged material viewed parallel to the forging direction (brighter tone represents CG, and darker tone represents UFG regions); **(b)** TEM bright field micrograph viewed normal to the forging direction*

The tensile behavior of a notched specimen of the as-forged bimodal alloy is shown in the nominal stress–nominal strain curve shown in Fig. 3. For comparison, engineering stress–strain curves for a 100% NC Al–7.5Mg alloy [16] and the conventional Al 5083 alloy [16] are also plotted in Fig. 3. The nominal stress was calculated by the applied load divided by the net cross-sectional area at the notches, and the nominal strain was obtained using the displacements divided by the gauge length regardless of the notches. Tensile tests using an unnotched standard specimen have revealed that the average yield strength of this material in the direction normal to the forging direction was 270 MPa [Newbery AP, Lavernia EJ, unpublished manuscript]. The tensile elongation of this material was ~7% [Newbery AP, Lavernia EJ, unpublished manuscript] in unnotched standard tests, and the notched specimen exhibited less ductility (~5% in Fig. 3) than unnotched specimen because of the plastic constraint at the notches.
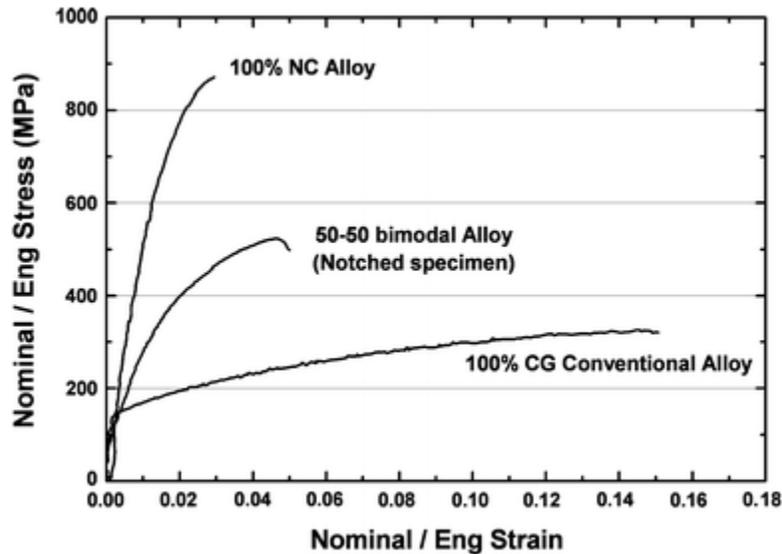
Fig. 3 *Nominal stress–strain behavior of the notched bimodal specimen, compared with engineering stress–strain curves of 100% NC Al–7.5Mg alloy [16] and conventional Al 5083 alloy [16]; 50–50 bimodal stands for a 50 wt.% CG and 50 wt.% NC/UFG bimodal material*

Figure 4 shows the strain field near a notch tip, as measured by DIC using a reference image and subsequent images after deformation. The images were recorded 30 s after the reference (~1.25×10^{-2} strain) and 1 s after the reference (~4.18×10^{-4} strain). The correlation shows that strain was highly concentrated near the notch tip, as shown in Fig. 4a, a natural consequence of the stress concentration at the root of the notch. A strain gradient was generated from the root of the notch toward the center of the specimen, with lobe orientations approximately 45° to the tension axis, where the resolved shear stress is a maximum. No significant strain variation was observed between UFG and CG regions in Fig. 4a. However, in the case of micro-strain in Fig. 4b, slight strain localizations were observed at scattered spots, which presumably coincided with CG regions.
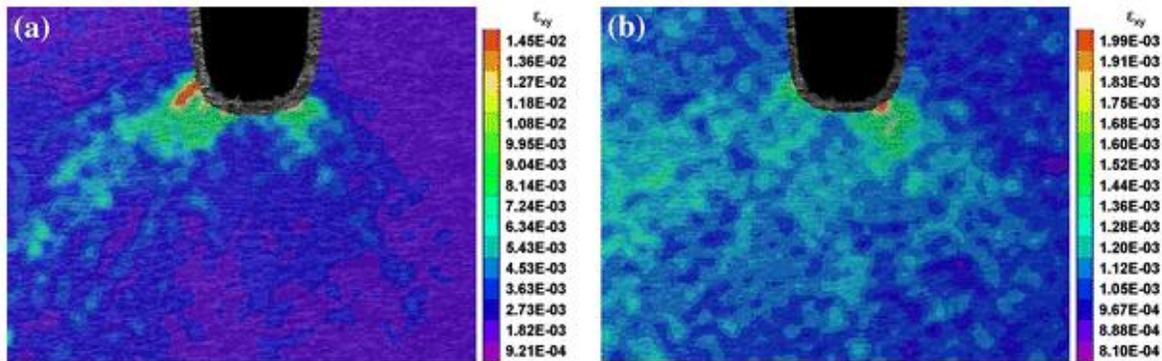
Fig. 4 *Displacement fields around a notch measured by DIC at different strains; (**a**) large strain (30 s interval) and (**b**) micro-strain (1 s interval)*

To investigate the strain localization in detail, another DIC was performed using two images taken at half-second intervals after yielding, approximately equivalent to a micro-strain of 2.09×10^{-4}, near the notches and at the central region between the two notches. Figure 5 shows light micrographs and the corresponding micro-strain contours for the bimodal structure at the two locations. The DIC results in Fig. 5 indicate that the strain is inhomogeneous between UFG and CG regions in both locations. The strain near the notches shown in Fig. 5a is overall greater than that between the notches in Fig. 5b, as one would expect. Also, UFG regions adjacent to CG bands were more highly strained near the notches compared with distant regions, a consequence of the higher stress concentration near the notches. For both locations, the strain is localized primarily within CG regions, indicating that the softer CG regions were more deformed than the harder UFG matrix. Therefore, more dislocations are generated within the CG regions, which undergo slip during the deformation. Dislocations glide more easily in CG regions on account of the lower density of obstacles (principally grain boundaries) in the larger grains. Conversely, the mobility of dislocations is limited within UFG regions because of the smaller grains. However, any strain differences between UFG and CG regions in micro-strain must be accommodated ultimately, since the total strain must be equal in both UFG and CG regions. (This was also shown in Fig. 4a by the absence

of contour variations between UFG and CG at large strains). Thus, different deformation mechanisms are involved in the UFG regions that ensure compatibility (equal strains) at the UFG–CG boundaries.

Several deformation mechanisms have been proposed for NC/UFG materials, ranging from dislocation plasticity to grain boundary sliding [7, 21, 22]. In the present study, the micro-crack initiation and development in UFG regions or at interfaces between CG and UFG regions might be responsible to compensate significant plastic strain in CG regions during tensile deformation and accommodate strain inhomogeneity between two regions. Concurrently, fast propagation of cracks through UFG regions can be delayed by plastic deformation and crack blunting in CG regions.
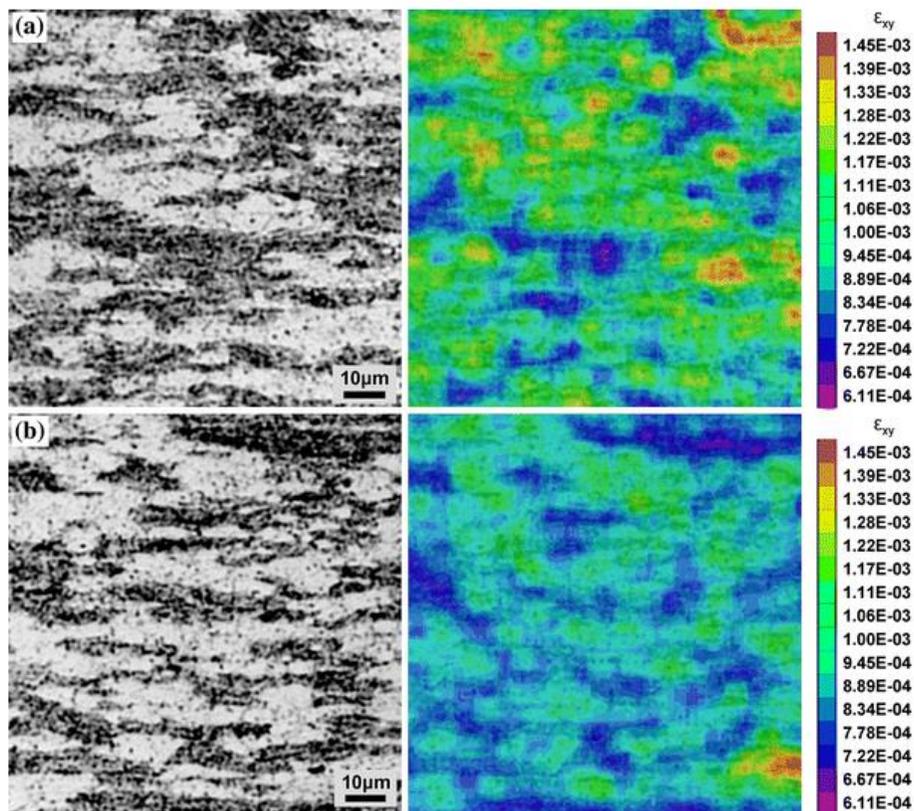

Fig. 5 *Optical micrographs and corresponding DIC results showing inhomogeneous strain measured from two locations; (**a**) near the notches and (**b**) central part between the notches*

Further evidence of inhomogeneous strain was manifest in Vickers hardness (Hv) values measured at the two different locations and within both UFG and CG regions. The measured Hv

values at each intermission (0, 182, 364, 455, and 515 MPa) during the tensile test are plotted in Fig. 6. The first comparison of Hv variation is between UFG and CG regions at the same location. In both locations, the Hv of CG regions increased more than that of the UFG regions as the applied stress increased, especially after the yielding (270 MPa). This implies that more strain hardening occurred in CG regions compared to the UFG regions during plastic deformation. This finding is consistent with the strain heterogeneity revealed by the DIC results. The difference in magnitude of the strain hardening between UFG and CG regions is attributed to the greater increase in dislocation density within CG regions, as well as the greater dislocation mobility. The density of dislocations significantly increased in CG regions after yielding, and the observed hardening arose from tangles of dislocations gliding on slip systems. The second comparison is between the two locations for UFG and CG. In this case, the increment in Hv of CG near the notches was greater than at the central part. Conversely, the variation in UFG Hv at the two locations was negligible. The stress concentration adjacent to the notch tips gave rise to these variations in both UFG and CG regions.
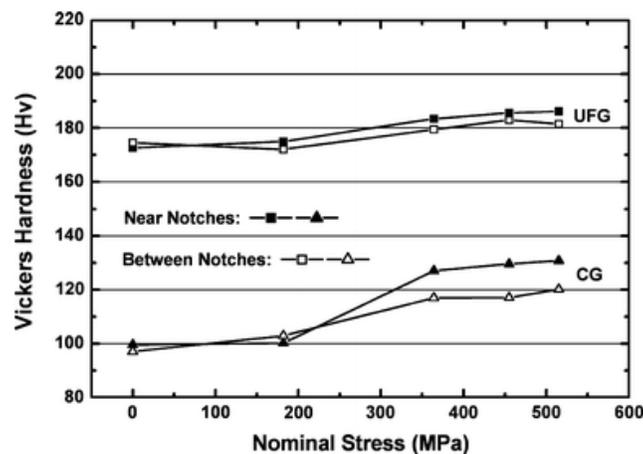

Fig. 6 *Local variations in strain hardening measured from both UFG and CG at two locations (near the notches and between the notches) with respect to the nominal tensile stress*

The tensile fracture surface of the as-forged material is shown in Fig. 7. In general, two different fracture surface morphologies were apparent: (i) a relatively brittle fracture surface comprising small dimples and (ii) a ductile fracture surface with large dimples. The former fracture surface (i) arose

from the fracture of UFG regions, a manifestation of the fact that the fracture becomes more brittle as grain size decreases. This phenomenon is also attributed to reduced mobility of dislocations. In UFG regions, dislocation glide distances were restricted by grain boundaries, limiting dislocation plasticity. The second fracture surface (ii) arose from the fracture of CG regions. The dimple size was typically between 1 and 4 μm, roughly equivalent to the CG size. In this case, the large surface dimples indicate that the CG regions underwent significantly more plastic strain than UFG regions. This can account for the nature of enhanced ductility in bimodal materials compared to 100% NC/UFG materials.
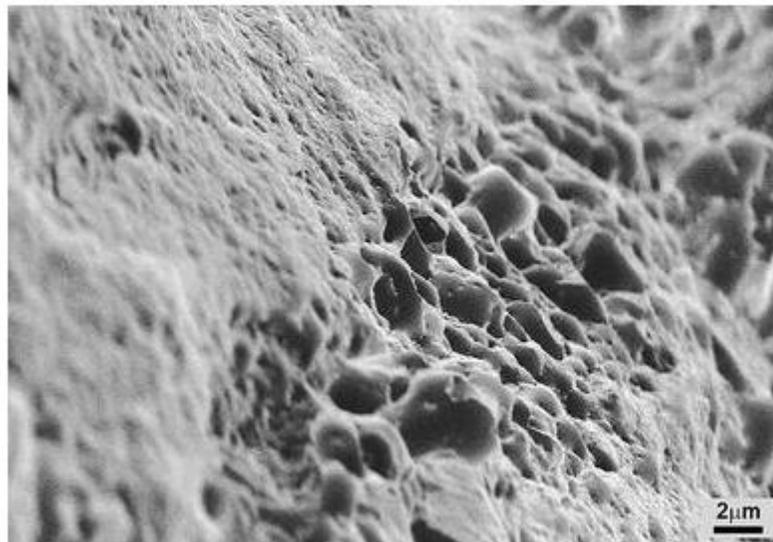

Fig. 7 *SEM micrograph of tensile fracture surfaces of the notched specimen*

4. Conclusions

A DIC technique was successfully applied to measure surface displacements during tensile deformation experiments. Strain inhomogeneity was observed between UFG and CG regions when the displacements were correlated in the micro-strain range. The strain localization in CG regions stemmed from the greater dislocation mobility in these regions compared to UFG regions. This

conclusion was supported by hardness measurements, which revealed different degrees of strain hardening during plastic deformation. The hardness variations between CG and UFG regions indicated a greater strain hardening effect in CG regions, an observation that was attributed to the increase in dislocation density and interactions. Strain mapping by DIC in this study, accompanied by dynamic observations, provides insights and understanding of deformation behavior of multi-scale materials.

References:

1. Gleiter H (1989) Prog Mater Sci 33:223. doi:10.1016/0079-6425(89)90001-7
2. Weertman JR, Averback RS (1996) In: Edelstein AS, Cammarata RC (eds) Nanomaterials: synthesis, properties and applications. Institute of Physics Publishing, Bristol, p 323
3. Newbery AP, Han BQ, Lavernia EJ, Suryanarayana C, Christodoulou JA (2007) In: Groza JR, Shackelford JF, Lavernia EJ, Powers MT (eds) Materials processing handbook. CRC Press, Boca Raton, FA, p 13–1
4. Hall EQ (1951) Proc Soc Lond B64:747
5. Petch NJ (1953) J Iron Steel Inst 174:25
6. Suryanarayana C (2001) Prog Mater Sci 46:1. doi:10.1016/ S0079-6425(99)00010-9
7. Witkin DB, Lavernia EJ (2006) Prog Mater Sci 51:1. doi: 10.1016/j.pmatsci.2005.04.004
8. Valiev RZ, Islamgaliev RK, Alexandrov IV (2000) Prog Mater Sci 45:103. doi:10.1016/S0079-6425(99)00007-9
9. Sanders PG, Fougere GE, Thompson LJ, Eastman JA, Weertman JR (1997) Nanostruct Mater 8:243. doi:10.1016/S0965-9773 (97)00167-0
10. Erb U (1995) Nanostruct Mater 6:533. doi:10.1016/0965-9773 (95)00114-X
11. Wang Y, Chen M, Zhou F, Ma E (2002) Nature 419:912. doi: 10.1038/nature01133
12. He G, Eckert J, Loser W, Schultz L (2002) Nat Mater 2:33. doi: 10.1038/nmat792
13. Tellkamp VL, Melmed A, Lavernia EJ (2001) Metall Mater Trans 32A:2335. doi:10.1007/s11661-001-0207-6
14. Youssef KM, Scattergood RO, Murty KL, Koch CC (2006) Scr Mater 54:251. doi:10.1016/j.scriptamat.2005.09.028
15. Han BQ, Lee Z, Witkin D, Nutt S, Lavernia EJ (2005) Metall Mater Trans 36A:957. doi:10.1007/s11661-005-0289-7

16. Lee Z, Witkin DB, Radmilovic V, Lavernia EJ, Nutt SR (2005) Mater Sci Eng A 410–411:462. doi:10.1016/j.msea.2005.08.104

17. Chan HW (1988) Mater Des 9:355

18. Newbery AP, Ahn B, Pao P, Nutt SR, Lavernia EJ (2007) Adv Mater Res 29–30:21

19. Sutton MA, Cheng M, Peters WH, Chao YJ, McNeill SR (1986) Image Vis Comput 4(3):143. doi:10.1016/0262-8856(86)90057-0

20. Ahn B, Newbery AP, Lavernia EJ, Nutt SR (2007) Mater Sci Eng A 463:61. doi:10.1016/j.msea.2006.07.158

21. Liao XZ, Zhou F, Lavernia EJ, Srinivasan SG, Baskes MI, He DW, Zhua YT (2003) Appl Phys Lett 83(4):632. doi:10.1063/ 1.1594836

22. Han BQ, Lavernia EJ (2005) Adv Eng Mater 7(6):457. doi: 10.1002/adem.200400219